

Transformer Network-based Reinforcement Learning Method for Power Distribution Network (PDN) Optimization of High Bandwidth Memory (HBM)

Hyunwook Park, Minsu Kim, Seongguk Kim, Keunwoo Kim, Haeyeon Kim, Taein Shin, Keeyoung Son, Boogyo Sim, *Student Member, IEEE*, Subin Kim, Seungtaek Jeong, Chulsoon Hwang, *Senior Member, IEEE* and Joungho Kim, *Fellow, IEEE*.

Abstract—In this article, for the first time, we propose a transformer network-based reinforcement learning (RL) method for power distribution network (PDN) optimization of high bandwidth memory (HBM). The proposed method can provide an optimal decoupling capacitor (decap) design to maximize the reduction of PDN self- and transfer impedance seen at multiple ports. An attention-based transformer network is implemented to directly parameterize decap optimization policy. The optimality performance is significantly improved since the attention mechanism has powerful expression to explore massive combinatorial space for decap assignments. Moreover, it can capture sequential relationships between the decap assignments. The computing time for optimization is dramatically reduced due to the reusable network on positions of probing ports and decap assignment candidates. This is because the transformer network has a context embedding process to capture meta-features including probing ports positions. In addition, the network is trained with randomly generated data sets. Therefore, without additional training, the trained network can solve new decap optimization problems. The computing time for training and data cost are critically decreased due to the scalability of the network. Thanks to its shared weight property, the network can adapt to a larger scale of problems without additional training. For verification, we compare the results with conventional genetic algorithm (GA), random search (RS), and all the previous RL-based methods. As a result, the proposed method outperforms in all the following aspects: optimality performance, computing time, and data efficiency.

Index Terms—Decoupling capacitor, Power distribution network (PDN), Reinforcement learning, Transformer network.

I. INTRODUCTION

RECENTLY, artificial intelligence (AI) era requires over the terabyte-per-second (TB/s) bandwidth between the processing units and memories in the AI server [1], [2]. To meet the demands, a graphic processing unit (GPU)–high bandwidth memory (HBM) module has been regarded as a promising solution. The GPU–HBM provides over several TB/s bandwidth between GPU and HBM with 1024 I/Os [3], [4].

This TB/s scale bandwidth is possible due to the silicon interposer and through silicon via (TSV) technologies [5], [6]. Those enable fine pitch interconnections and high density in the I/O interface. However, due to the increasing data rate from 1 Gbps at gen 1 to 6.4 Gbps at gen 3 and the tremendous number of I/Os, switching power in the HBM I/O interface has been increased by generations [7], [8]. Moreover, the supply voltage level keeps shrinking to limit the power consumption [3]. Therefore, robust power distribution network (PDN) design becomes further challenging. It is essential to ensure signal quality by lowering power supply noise (PSN) fluctuation and power supply induced jitter (PSIJ) [9]–[11].

Decoupling capacitor (decap) design is one of the most important processes to suppress PSN and PSIJ by lowering PDN impedance [12]. Simultaneous switching noise (SSN) is the main noise source in the HBM I/O interface, which leads to severe eye distortion as shown in Fig. 1 [13], [14]. Large SSN can be generated when the simultaneous switching current drawn by I/O buffers meets the high peak anti-resonances of the VDDQ PDN. Therefore, it is necessary to optimize decap design to lower the PDN impedance in the broadband frequency range while minimizing the layout area to reduce the process cost as well as the power consumption [15]–[17].

However, decap design optimization is a combinatorial optimization problem that has high computational complexity. This is because the previous decap assignment affects the next assignment in terms of PDN impedance reduction [18]. Moreover, a large scale of the PDN decap optimization requires extremely high computing cost. Because the size of PDN Z-matrix to be optimized is increased proportional to the square of the number of ports and proportional to the number of frequency points and data set size. In addition, the decap optimization requires high computing time since the computation of the PDN impedance is time-consuming. Also, massive iterations are needed for optimization. Therefore, a computing time and cost-effective methodology that is suitable

This article is an expanded version from the IEEE Electrical Design of Advanced Packaging and Systems (EDAPS), Shenzhen, China, December 14–16, 2020.

H. Park, M. Kim, S. Kim, K. Kim, T. Shin, H. Kim, K. Son, B. Sim and J. Kim are with the School of Electrical Engineering, Korea Advanced Institute of Science and Technology, Daejeon 34141, South Korea (e-mail: hyunwookpark@kaist.ac.kr; min-su@kaist.ac.kr; seonggukkim@kaist.ac.kr;

keunwookim@kaist.ac.kr; taeinshin@kaist.ac.kr; haeyeonkim@kaist.ac.kr; keeyoung@kaist.ac.kr; boogyo@kaist.ac.kr; joungho@kaist.ac.kr).

S. Kim is with Samsung Electronics, Suwon, 16677, South Korea (email: subinn.kim@samsung.com)

S. Jeong and C. Hwang is with Missouri University of Science and Technology, Rolla, MO, 65409, USA (email: sjeong@mst.edu; hwangc@mst.edu).

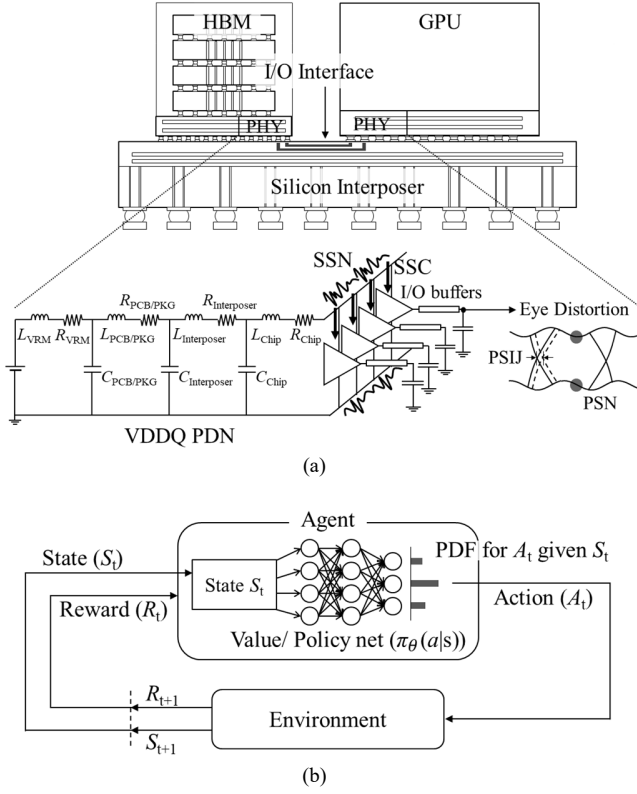


Fig. 1. (a) Eye distortion due to the large SSN generated by the numerous switching I/Os in the HBM-GPU I/O interface. (b) Reinforcement learning to solve combinatorial optimization problems defined by MDP parameters.

for combinatorial optimization considering previous decap assignments is needed.

Various decap optimization methods have been investigated based on the conventional genetic algorithm (GA) [12], [16], [19]. However, the previous GA-based methods cannot capture sequential combinatorial relationships between the decap assignments which limits the optimality performance. Also, those cannot capture meta-features over problems such as the position of probing ports. Whenever a new problem is given, those must re-optimize it which requires massive iterations. Therefore, their lack of reusability causes an increment of the optimization time.

Recently, machine learning has been introduced for decap optimization [20]. Especially, RL-based methods are being actively studied [21]–[28]. As shown in Fig. 1(b), the RL is an algorithm to solve the problem defined by Markov decision process (MDP) parameters – state, action, reward, and policy [29]. The main goal of the RL is to learn the policy which determines the action for the given state, to maximize the reward by interaction with the environment. If the neural network is used to approximate scalar value functions and the policy is totally determined by the value function, it is called value-based RL and the network is a value network. If the network directly parameterizes the policy as probability distribution functions (PDFs), it is called policy-based RL and the network is a policy network. Deep Q learning-based on-board decap optimization methods using a multi-layer

perceptron (MLP) as the value function approximator are investigated [23], [25]. Also, on-interposer and on-chip decap optimization using deep Q learning with a convolutional neural network (CNN) is studied [24]. However, those are limited in both the size of the solution space and the optimality performance. Because they are based on the value-based RL algorithms with simple value approximators such as the MLP and CNN. To increase the solution space size, direct policy parameterization by policy networks and training the networks through policy gradient algorithms are investigated [26], [27]. In addition, [27] introduced a transformer network to consider sequential relationships between the decap assignments for performance improvement. However, both of them do not have the reusability causing the increment of the optimization time. A recent study proposed a reusable method on the position of the probing port [28]. However, all the previous RL-based methods including [28] are limited in scalability which causes the increment of computing time and cost when training [21]–[28]. The scalability refers to the characteristic of whether the trained neural network model can respond to the scale of the problem. Moreover, all the previous RL-based methods only considered self-impedance for the design metric. Those exclude transfer impedance which indicates the coupled PSN [21]–[28]. In addition, multi-probing ports are not considered [21]–[25], [27], [28].

In this article, we propose a transformer network-based RL method for PDN decap optimization of the HBM. The proposed method can optimize decap design to maximize the reduction of both the self- and transfer impedance seen at the multiple ports. Consideration of the sequential relationships between the decap assignments using the transformer network achieves higher optimality performance. Moreover, the network has a context embedding process to capture meta-feature including positions of probing ports. The context embedding process increases the generalization ability to new problems. Therefore, the network trained with randomly generated data sets is reusable to new problems varying positions of probing ports and decap candidates. Due to the shared weight property, the network has the generalization ability on the scale of decap optimization problems. The reusability and scalability provide a significant reduction of the computing time and cost for both the training and optimization. By comparing with the conventional GA and RS methods and all the previous RL-based methods in [21]–[28], we validate the higher optimality and the lower computing cost and time.

II. PROPOSAL OF TRANSFORMER NETWORK-BASED RL METHOD FOR PDN DECOUPLING CAPACITOR OPTIMIZATION

In this section, a transformer network-based RL method for the PDN decap optimization is proposed. A brief explanation of the decap optimization problem for this work is as follows. It is denoted as a decap n/m problem. The problem formulation of the decap n/m is as follows: assigning m number of unit NMOS decaps for given n number of positions for decap assignment candidates x to maximize the reduction of the self- and transfer impedance seen at 4 probing ports p . The decap assignment

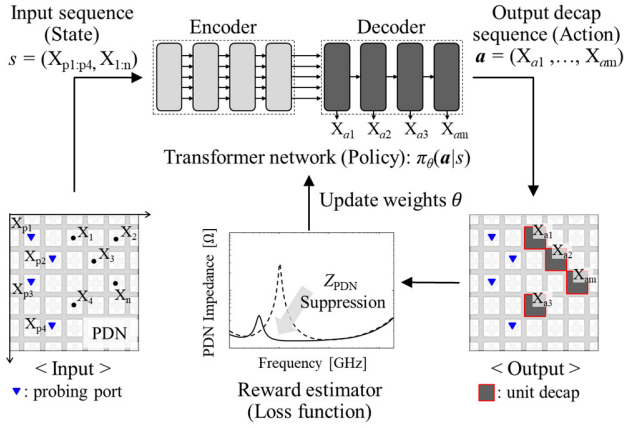


Fig. 2. Proposal of transformer network-based reinforcement learning method for PDN decap optimization.

candidates \mathbf{x} is a set of features of n ports from on-chip and on-interposer HBM VDDQ PDN:

$$\mathbf{x} = (X_1, X_2, X_3, \dots, X_n). \quad (1)$$

\mathbf{p} is a set of 4 probing ports in the I/O region of a physical layer (PHY) of the on-chip VDDQ PDN:

$$\mathbf{p} = (X_{p1}, X_{p2}, X_{p3}, X_{p4}). \quad (2)$$

Therefore, a total 10 number of the self- and transfer impedances become a decap design criterion: $Z_{11}, Z_{22}, Z_{33}, Z_{44}, Z_{12}, Z_{13}, Z_{14}, Z_{23}, Z_{24}$ and Z_{34} .

Fig. 2 shows the overall concept of the proposed transformer network-based RL method for the PDN decap optimization. For a given input state s , a policy network outputs a decap assignment sequence \mathbf{a} . The MDP parameters are defined as follows: State s is a set of feature vectors (\mathbf{X} 's) of the probing ports ($X_{p1:p4}$) and the decap assignment candidates ($X_{1:n}$); Action \mathbf{a} is deriving a decap assignment sequence ($X_{a1:am}$); Reward r is modeled based on the reduction of the self- and transfer impedance compared to the initial PDN. The policy network is an encoder-decoder transformer network that is based on an attention mechanism [30]. The network directly parameterizes the probability distributions $\pi_\theta(\mathbf{a}|s)$ of the action for the given state by the weights θ . Details on the definition of MDP parameters and the attention-based transformer network are explained in Section II-A and II-B respectively. The loop in Fig. 2 – input state goes into the transformer network; the network outputs the decap assignment sequence; estimating the loss function of the PDN with assigned unit decaps by the reward estimator; updating the weight θ by the policy gradient algorithm to minimize the loss function – is iterated to optimize the policy network. Details on the training process of the network are described in Section II-C.

The network has the context embedding process to capture the meta-feature of the positions of the probing ports. The context embedding process increases the generalization ability to new problems varying locations of the probing ports and the decap candidates. Details on the context embedding are explained in Section II-B. Moreover, the policy network is trained with randomly generated data sets for reusability. The

data sets are the states and corresponding PDN Z-matrices, with randomly generated locations for probing ports and decaps. Details on the randomly generated data are described in Section II-D. The computing time for the RL-based methods is composed of training time to train the network and optimization time to obtain the optimized results. The reusability can reduce the optimization time because only one inference and one reward estimation are required without additional training for a new input.

The network has scalability on both the number of the decap candidates n and that of the decap assignments m . The n is also called the size of the action space. The scalability is due to the shared weight properties of the encoder and decoder network. Details on the shared weight property are mentioned in Section II-B. The scalability can reduce the training time. Because the policy network trained in the smaller scale of the decap problems can be used to solve the larger scale of problems. Most of the training time is consumed in the impedance calculation by cascading the Z-matrices of PDN and decaps. Therefore, the size of those directly affects the training time. If the encoder has scalability, the size of PDN Z-matrix data for training can be reduced. Because the number of the ports for the decap candidates is decreased. If the decoder has scalability, the size of the cascaded Z-matrix of the unit decap array can be reduced.

A. Markov Decision Process (MDP) for PDN Decap Design

Fig. 3 shows the detailed explanation of the MDP parameters – state s , action \mathbf{a} and reward r . Fig. 3(a) is the top view of the HBM VDDQ PDN. The PDN environment is configured of a 3-dimensional grid world, which is divided by $375 \times 375 \mu\text{m}^2$ unit-decap sized unit cells (UDUCs).

The state s is defined as a set of 4-dimensional vectors \mathbf{X} 's of 4 probing ports \mathbf{p} and n number of the decap assignment candidates. The 4 probing ports \mathbf{p} are denoted in blue triangles and the n decap candidates are in black circles in Fig. 3(a). Each \mathbf{X} contains x -, y -, z - coordinates and whether the port is the probing port or not:

$$s = (\mathbf{p}, \mathbf{x}) = (X_{p1:p4}, X_{1:n}) \quad (3)$$

$$X_i = (x\text{-coord}, y\text{-coord}, z\text{-coord}, isProbingPort).$$

where $i \in \{p1:p4, 1:n\}$ indicates a node index.

The action \mathbf{a} is defined as deriving out the m size of the decap assignment sequence as depicted in the red circles in Fig. 3(a). Therefore, it can be expressed as the permutation of sub-actions a_i :

$$\mathbf{a} = (a_{i=1}, a_{i=2}, \dots, a_{i=m}) = (X_{a1}, X_{a2}, \dots, X_{am}) \quad (4)$$

$$X_{ak} \in \mathbf{x}, k \in \{1:m\}.$$

The sub-action a_i is defined as assigning a unit decap at a certain position X_{ak} at the time-step t . X_{ak} 's are elements of \mathbf{x} . The unit decap is a $375 \times 375 \mu\text{m}^2$ sized NMOS decap with 1.055 nF capacitance and 0.7 mΩ equivalent series resistance (ESR). It is modeled based on the TSMC 65 nm process. Details on the modeled NMOS decap are described in Section III.

The reward r is defined as a sum of the weighted mean of the

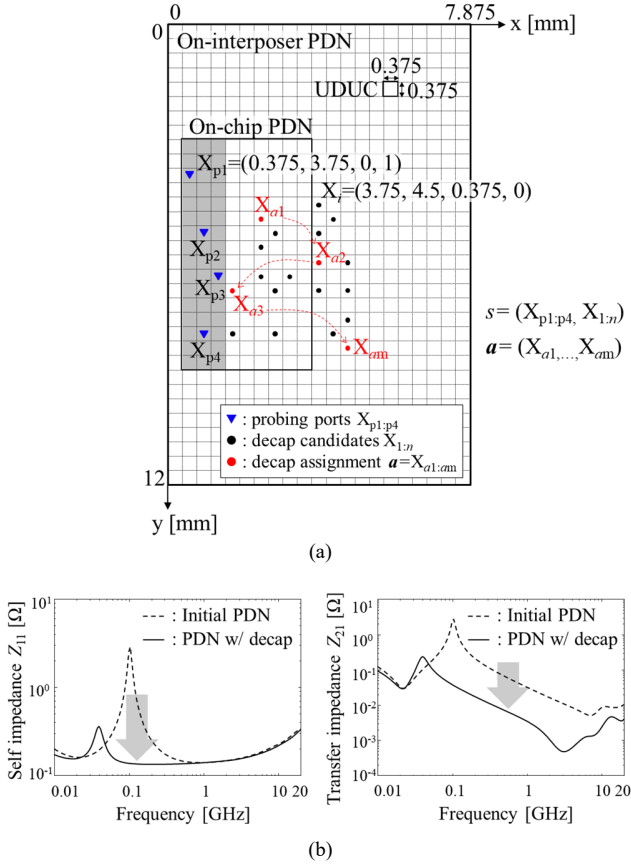


Fig. 3. Defined MDP parameters. (a) State s and Action a . (b) Reward r .

self- and transfer impedance reduction at the 4 probing ports p :

$$r(a|s) = \alpha_r \times \sum_p \sum_f (|Z_{11_initial}(f)| - |Z_{11_wDecap}(f)|) / 4 + (1 - \alpha_r) \times \sum_p \sum_f (|Z_{21_initial}(f)| - |Z_{21_wDecap}(f)|) / 6. \quad (5)$$

where α_r is the coefficient of the self-impedance reduction ($=0.7$ for this work). f is a set of 166 frequency points from 10 MHz to 20 GHz. $Z_{11_initial}$ and Z_{11_wDecap} are the self-impedances seen at p of initial PDN and the PDN with decaps respectively; $Z_{21_initial}$ and Z_{21_wDecap} are the transfer-impedances seen at p of the initial PDN and the PDN with decaps respectively, as shown in Fig. 3(b).

The policy $\pi_\theta(a|s)$ is defined as a PDF of the output decap assignment sequence a for the given state s . Since the action a is represented by the permutation of sub-actions a_t , it can be factorized by the PDFs of sub-actions $p_\theta(a_t|s, a_{1:t-1})$:

$$\pi_\theta(a|s) = \prod_{t=1}^m p_\theta(a_t|s, a_{1:t-1}). \quad (6)$$

B. Attention-based Encoder-decoder Transformer Network for Policy Approximation

The policy $\pi_\theta(a|s)$ is approximated by the encoder-decoder transformer network as depicted in Fig. 4(a). Hence, the parameter θ of π_θ becomes the weights of the transformer network. The main mechanism of the network is the attention. By the attention computation, the encoder embeds the input state s into high-dimensional node embeddings h and the

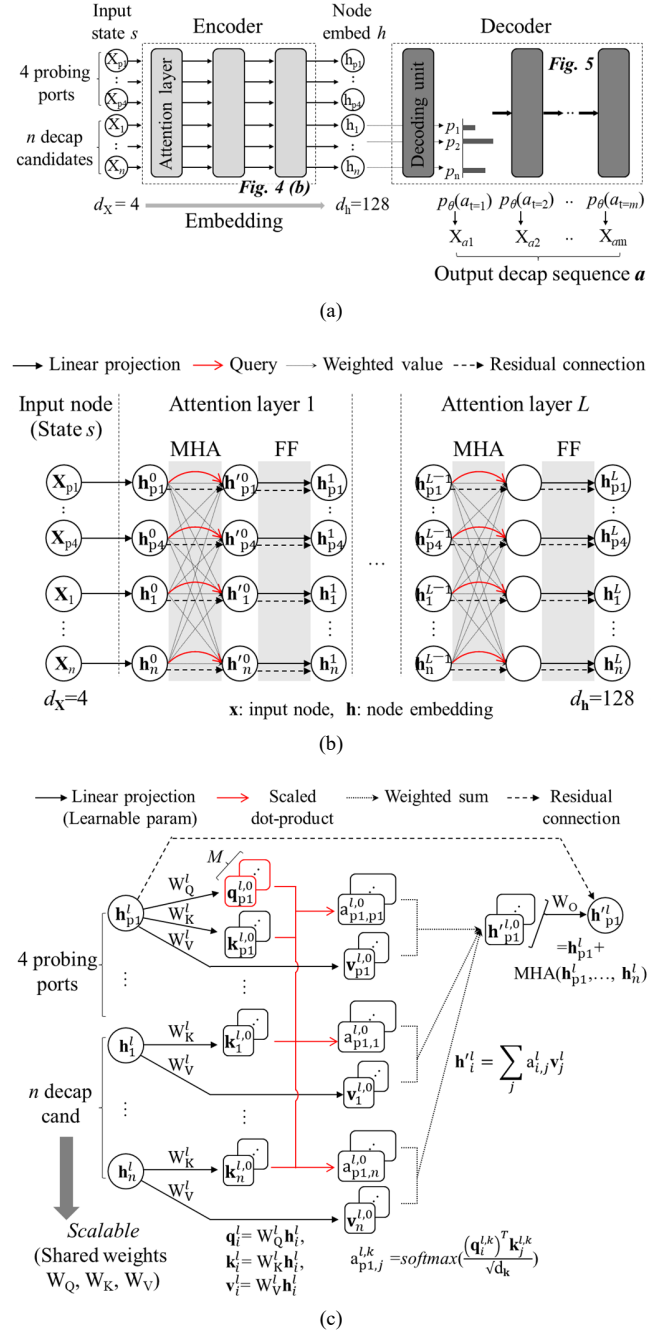


Fig. 4. (a) Encoder-decoder transformer network for policy approximation. (b) Encoder transformer network for embedding input state s into high-dimensional node embeddings h . (c) Details of the attention layer of the encoder – MHA sublayer with skip connection.

decoder provides output decap sequence a by computing the PDF of next unit decap assignment $p_\theta(a_t)$.

The attention mechanism is a weighted value passing algorithm between nodes to capture their relationships [31]. Every node can have query q , key k and value v . The q is the object for questioning to the neighbor nodes and k is the description or characteristic for each node [30]. Therefore, each node can compute its compatibility u to the neighbor nodes by scale-dot product of its q and k of the neighbor nodes [31, eq.

(11)]. The attention weight \mathbf{a} is computed by taking softmax function to \mathbf{u} [30, eq. (1), 31, eq. (12)]. Finally, by using the attention weight \mathbf{a} , the next \mathbf{h} can be embedded as the weighted sum of \mathbf{v} of every node [31, eq. (13)]. Therefore, relationships between nodes can be captured in \mathbf{h} . This computation is called a scaled dot-product attention or single head attention (SHA). A multi-head attention (MHA) is a parallel computation of scaled-dot product attention to learn diverse representation [30]. With M sets of linear projected \mathbf{q} , \mathbf{k} and \mathbf{v} , each head is calculated through SHA. Finally, the concatenated M number of heads are linearly projected to the final node embedding \mathbf{h} .

The main purpose of the encoder transformer network is to embed relationships between the 4 probing ports \mathbf{p} and the n decap candidates into \mathbf{h} – the 4-dimensional input state s ($d_x=4$) to 128-dimensional \mathbf{h} ($d_h=128$). Fig. 4(b) shows the details of the encoder transformer network. Initial node embedding \mathbf{h}_i^0 is embedded by the linear projection of input node X_i :

$$\mathbf{h}_i^0 = \mathbf{W}_X X_i + \mathbf{b}_X. \quad (7)$$

where $i \in \{p1:p4, 1:n\}$ indicates the node index; $\mathbf{W}_X \in \mathbb{R}^{d_h \times d_x}$ and $\mathbf{b}_X \in \mathbb{R}^{d_h}$ are learnable parameters. The node embeddings \mathbf{h}_i^l of the layer l are updated sequentially by attention layers. The encoder is configured of L number of the attention layers. Each of them consisted of one MHA sublayer and one feed-forward (FF) sublayer with residual connections [31]:

$$\mathbf{h}_i^l = \mathbf{h}_i^l + \text{MHA}^l(\mathbf{h}_{p1}^l, \dots, \mathbf{h}_{p4}^l, \mathbf{h}_1^l, \dots, \mathbf{h}_n^l) \quad (8-1)$$

$$\mathbf{h}_i^{l+1} = \mathbf{h}_i^l + \text{FF}^l(\mathbf{h}_i^l). \quad (8-2)$$

where $l \in \{1:L\}$ indicates the layer index. \mathbf{h}_i^l is the output of a MHA sublayer; \mathbf{h}_i^{l+1} is the output of a FF sublayer. The residual connection means $x + f(x)$ for preventing the gradient vanishing [32]. The FF sublayer has one hidden layer with the dimension d_{ff} , hence there are 4 learnable parameters $\mathbf{W}_{ff,1}$, $\mathbf{b}_{ff,1}$, $\mathbf{W}_{ff,2}$, and $\mathbf{b}_{ff,2}$. A ReLU activation is used for the FF sublayer. Especially in the MHA sublayer of the encoder, all the nodes have their own queries which are denoted in the red lines as shown in Fig. 4(b). This is for all the nodes to capture their relationships with each other through the attention.

Fig. 4(c) shows the details of the MHA sublayer. It shows how the node embedding of the first probing port \mathbf{h}_{p1}^l is updated by the MHA – graphical explanation of (8-1). First of all, each node embedding generates its query $\mathbf{q}^{l,k}$, key $\mathbf{k}^{l,k}$ and value $\mathbf{v}^{l,k}$ by linear projection with learnable parameters $\mathbf{W}_Q^{l,k}$, $\mathbf{W}_K^{l,k}$ and $\mathbf{W}_V^{l,k}$:

$$\mathbf{q}_i^{l,k} = \mathbf{W}_Q^{l,k} \mathbf{h}_i^l, \mathbf{k}_i^{l,k} = \mathbf{W}_K^{l,k} \mathbf{h}_i^l, \mathbf{v}_i^{l,k} = \mathbf{W}_V^{l,k} \mathbf{h}_i^l. \quad (9)$$

where $k \in \{1, \dots, M\}$ indicates a head index. M is the number of heads. d_k and d_v are the dimensions of key and value. $\mathbf{W}_Q^{l,k} \in \mathbb{R}^{d_k \times d_h}$, $\mathbf{W}_K^{l,k} \in \mathbb{R}^{d_k \times d_h}$ and $\mathbf{W}_V^{l,k} \in \mathbb{R}^{d_v \times d_h}$ are the learnable parameters to make each head, hence $\mathbf{W}_Q^l, \mathbf{W}_K^l \in \mathbb{R}^{Md_k \times d_h}$ and $\mathbf{W}_V^l \in \mathbb{R}^{Md_v \times d_h}$. After the query, the key and value are computed, attention weights $a_{p1,j}^{l,k}$ between the first probing node and other nodes are calculated in parallel:

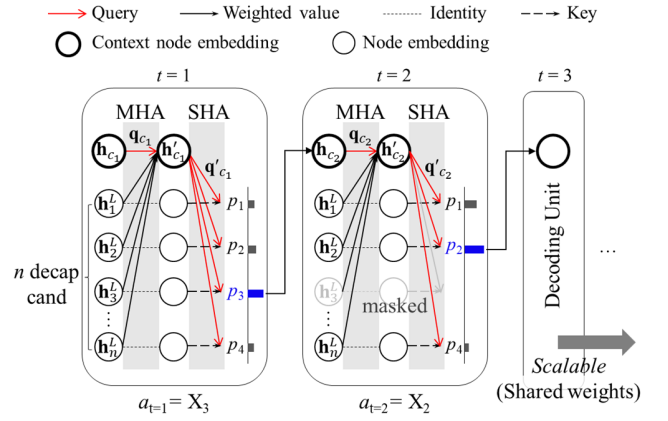


Fig. 5. Decoder transformer network providing the decap assignment sequence \mathbf{a} by computing the PDF of the next unit decap assignment.

$$a_{p1,j}^{l,k} = \text{softmax}\left(\frac{(\mathbf{q}_{p1}^{l,k})^T \mathbf{k}_j^{l,k}}{\sqrt{d_k}}\right). \quad (10)$$

where $j \in \{p1:p4, 1:n\}$ indicates the node index. Then, each head $\mathbf{h}_{p1}^{l,k}$ is computed by the weighted sum of the values by the attention weight:

$$\mathbf{h}_{p1}^{l,k} = \sum_j a_{p1,j}^{l,k} \mathbf{v}_j^l. \quad (11)$$

where $j \in \{p1:p4, 1:n\}$ indicates the node index. Finally, all the heads are concatenated and linearly projected back into d_h dimension by a learnable parameter $\mathbf{W}_O^l \in \mathbb{R}^{d_h \times Md_v}$. Also, the residual connection is added:

$$\mathbf{h}_{p1}^l = \mathbf{W}_O^l \text{Concat}(\mathbf{h}_{p1}^{l,1}, \dots, \mathbf{h}_{p1}^{l,M}) + \mathbf{h}_{p1}^l. \quad (12)$$

where Concat is the concatenation operation.

Unlike the MLP or CNN as approximators in the previous works [23]–[26], all the learnable parameters \mathbf{W}_X , \mathbf{b}_X , \mathbf{W}_Q^l , \mathbf{W}_K^l , \mathbf{W}_V^l , $\mathbf{W}_{ff,1}$, $\mathbf{b}_{ff,1}$, $\mathbf{W}_{ff,2}$ and $\mathbf{b}_{ff,2}$ are shared for each node in the same sublayer as depicted in Fig. 4(c). Therefore, the encoder transformer network is scalable on the number of the decap candidate nodes n . Because the nodes can be easily added without re-defining the learnable parameters.

Fig. 5 shows the details of the decoder transformer network. The main purpose of the decoder is to provide the decap assignment sequence \mathbf{a} . The decoder consists of the m number of decoding units which is equal to the size of \mathbf{a} . Each decoding unit computes the PDF $p_\theta(a_t | s, a_{1:t-1})$ of the next unit decap assignment and outputs the position of the next assignment. A decoding unit is configured of one MHA layer and one SHA layer. Unlike the encoder, only context node embeddings \mathbf{h}_{c_t} and \mathbf{h}'_{c_t} become queries \mathbf{q}_{c_t} and \mathbf{q}'_{c_t} . Then, $p_\theta(a_t | s, a_{1:t-1})$ is computed by the attention with keys from the encoder output node embeddings of the decap candidates. Especially, the node embedding of the previous decap assignment is included in \mathbf{h}_{c_t} at every time-step as shown in Fig. 5. Therefore, the previous assignment can be considered to determine the next assignment. This is how the proposed method can capture the sequential

combinatorial relationship between the decap assignments.

Since the context node embedding \mathbf{h}_{c_t} becomes the query and determines the policy for the next decap assignment, it is a key factor in the decoder. Hence, the context node embedding is defined as the following:

$$\mathbf{h}_{c_t} = \text{Concat}(\mathbf{h}_{a_{t-1}}^L, \mathbf{h}_{p_1}^L, \mathbf{h}_{p_2}^L, \mathbf{h}_{p_3}^L, \mathbf{h}_{p_4}^L, \bar{\mathbf{h}}^L) \quad (13)$$

where $\mathbf{h}_{a_{t-1}}^L$ indicates the node embedding of the previous decap assignment. $\mathbf{h}_{p_1}^L, \mathbf{h}_{p_2}^L, \mathbf{h}_{p_3}^L$ and $\mathbf{h}_{p_4}^L$ indicate node embeddings of 4 probing ports \mathbf{p} . $\bar{\mathbf{h}}^L$ is the mean of all the node embeddings. The dimension of the context node d_{hc} equals to $d_h \times 6$. Therefore, not only the previous assignment, but also the positions of the probing ports can be considered when determining the next assignment.

Details on the PDF computation for the next assignment are as follows. First, a new context node embedding \mathbf{h}_{c_t} is calculated in the MHA layer – The \mathbf{q}_{c_t} projected from \mathbf{h}_{c_t} ; \mathbf{k} and \mathbf{v} from the encoder output node embeddings of the decap candidates $\mathbf{h}_1^L, \dots, \mathbf{h}_n^L$:

$$\begin{aligned} \mathbf{h}_{c_t}' &= \text{MHA}(\mathbf{h}_{c_t}, \mathbf{h}_1^L, \dots, \mathbf{h}_n^L) \\ \mathbf{q}_{c_t} &= \mathbf{W}_Q \mathbf{h}_{c_t}, \mathbf{k}_i = \mathbf{W}_K \mathbf{h}_i^L, \mathbf{v}_i = \mathbf{W}_V \mathbf{h}_i^L. \end{aligned} \quad (14)$$

where $\mathbf{W}_Q \in \mathbb{R}^{Md_k \times d_{hc}}$, $\mathbf{W}_K \in \mathbb{R}^{Md_k \times d_h}$ and $\mathbf{W}_V \in \mathbb{R}^{Md_v \times d_h}$ are the learnable parameters. $i \in \{1:n\}$ indicates the node index of the decap candidates. Then, the compatibility u is computed by scaled dot-product between \mathbf{q}_{c_t}' and \mathbf{k}' . The \mathbf{q}_{c_t}' is projected from \mathbf{h}_{c_t}' , and the \mathbf{k}' is from $\mathbf{h}_1^L, \dots, \mathbf{h}_n^L$:

$$\begin{aligned} \mathbf{q}_{c_t}' &= \mathbf{W}_Q' \mathbf{h}_{c_t}', \mathbf{k}_i' = \mathbf{W}_K' \mathbf{h}_i^L \\ u_i &= \begin{cases} C \tanh \left(\frac{(\mathbf{q}_{c_t}')^T \mathbf{k}_i'}{\sqrt{d_k'}} \right) & \text{if } i \neq a_{t'} \\ -\infty & \text{otherwise.} \end{cases} \quad \forall t' < t \end{aligned} \quad (15)$$

where $\mathbf{W}_Q', \mathbf{W}_K' \in \mathbb{R}^{d_k' \times d_{hc}}$ are the learnable parameters. $i \in \{1:n\}$ indicates the node index of the decap candidates. d_k' is a dimension of the key in the SHA layer. C is a tanh clipping [33]. Selecting the locations of the previous assignments is masked by making the u be negative infinity. Finally, $p_\theta(a_t|s, a_{1:t-1})$ is provided as the softmax of the u :

$$p_\theta(a_t = X_i | s, a_{1:t-1}) = p_i = \frac{e^{u_i}}{\sum_{j=1}^n e^{u_j}}. \quad (16)$$

where $i \in \{1:n\}$ indicates the node index of the decap candidates.

Based on the estimated PDF p_θ , there are two decoding strategies: greedy and sampling. The greedy selection is to choose the position where the probability is maximized – selecting the best action. The sampling selection is to choose according to the estimated PDF. In the training phase, only the sampling is used to balance exploration and exploitation because the agent cannot distinguish which is the decent action

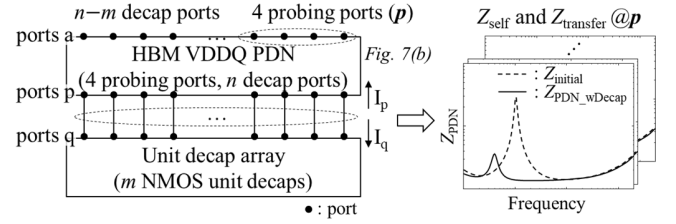


Fig. 6. Reward estimator to compute impedance of decap assigned PDN by cascading Z-matrix of HBM VDDQ PDN and that of unit decap array.

in the beginning of the training [29]. In the optimization phase, both the greedy and sampling selection can be used. The greedy can reduce the computing cost and time since only one inference and reward evaluation are required. However, the optimality performance is worse than that of the sampling. In the sampling selection, the computing time and cost are increased as much as a multiple of the sampling width. However, the optimality performance is higher than that of the greedy because the best solution is selected among the sampled solutions.

The decoder provides scalability on the number of the decap assignments m as shown in Fig. 5. This is because all the learnable parameters $\mathbf{W}_Q, \mathbf{W}_K, \mathbf{W}_V, \mathbf{W}_Q'$ and \mathbf{W}_K' are shared for each decoding unit.

C. Training Algorithm and Loss Function Calculation by the Reward Estimator

The policy gradient algorithm REINFORCE is used for training the policy network [34]. The loss function $\mathcal{L}(\theta|s)$ is the criterion for updating the weights of the network. Hence, it should evaluate the performance of the assigned decaps. The loss function $\mathcal{L}(\theta|s)$ is defined as the expectation of a cost function $L(\mathbf{a})$ which is defined as the negative reward:

$$\mathcal{L}(\theta|s) = \mathbb{E}_{\pi_\theta(\mathbf{a}|s)}[L(\mathbf{a})] = \mathbb{E}_{\pi_\theta(\mathbf{a}|s)}[-r(\mathbf{a}|s)]. \quad (17)$$

As shown in Fig. 6, the reward $r(\mathbf{a}|s)$ is calculated by the reward estimator which computes the impedance of the decap-assigned PDN. The reward estimator performs cascading the Z-matrix of the VDDQ PDN Z_{PDN} and that of the decap array Z_{da} consisting of m unit decaps. The cascaded ports are the ports p and q in Z_{PDN} and Z_{da} respectively; the ports a are the remaining ports of Z_{PDN} . The cascaded PDN Z-matrix Z_{PDN_wDecap} is calculated using boundary conditions on the ports p and q [35, eqs. (1)–(3)].

Based on the defined $\mathcal{L}(\theta|s)$, the gradient of the loss function $\nabla_\theta \mathcal{L}(\theta|s)$ can be derived as the following equation [29], [34]:

$$\nabla_\theta \mathcal{L}(\theta|s) = \mathbb{E}_{\pi_\theta(\mathbf{a}|s)}[(L(\mathbf{a}) - L(\mathbf{a}_{BL}))] \nabla_\theta \log \pi_\theta(\mathbf{a}|s). \quad (18)$$

where $L(\mathbf{a}_{BL})$ is the cost function estimated by the rollout baseline θ^{BL} [31]. The baseline network has the same configuration as the transformer policy network. It is periodically updated after every epoch if the improvement is critical according to a paired t-test [31]. The reason why subtracting the baseline is to reduce variance when training [29]. Finally, the learnable parameter θ of the policy network is

Algorithm 1 Training via REINFORCE with rollout baseline (decap n/m)

Inputs: action space size n , number of epochs E , steps per epoch T , batch size B , validation size V , full-ports PDN Z-matrix Z_{fp} , m -sized decap array Z-matrix Z_{da}

```

Initialize  $\theta, \theta^{BL}$ 
for epoch = 1 to  $E$  do
  for step = 1 to  $T$  do
     $s_i, Z_{si} \leftarrow \text{RandomDataGen}(n, Z_{fp}) \forall i \in \{1, \dots, B\}$ 
     $a_i \leftarrow \text{SampleInference}(s_i, \pi_\theta) \forall i \in \{1, \dots, B\}$ 
     $a_i^{BL} \leftarrow \text{GreedyInference}(s_i, \pi_{\theta^{BL}}) \forall i \in \{1, \dots, B\}$ 
     $r_i \leftarrow \text{RewardEst}(a_i, s_i, Z_{si}, Z_{da}) \forall i \in \{1, \dots, B\}$ 
     $r_i^{BL} \leftarrow \text{RewardEst}(a_i^{BL}, s_i, Z_{si}, Z_{da}) \forall i \in \{1, \dots, B\}$ 
     $\nabla_\theta \mathcal{L} \leftarrow \sum_{i=1}^B (L(a_i) - L(a_i^{BL})) \nabla_\theta \log(\pi_\theta(a_i))$ 
     $\theta \leftarrow \text{Adam}(\theta, \nabla_\theta \mathcal{L})$ 
  end for
   $s_j, Z_{sj} \leftarrow \text{RandomDataGen}(n, Z_{fp}) \forall j \in \{1, \dots, V\}$ 
   $a_j \leftarrow \text{GreedyInference}(s_j, \pi_\theta) \forall j \in \{1, \dots, V\}$ 
   $a_j^{BL} \leftarrow \text{GreedyInference}(s_j, \pi_{\theta^{BL}}) \forall j \in \{1, \dots, V\}$ 
  if PairedTTest( $\pi_\theta(a)$ ,  $\pi_{\theta^{BL}}(a^{BL})$ ) < 0.05 then
     $\theta^{BL} \leftarrow \theta$ 
  end if
end for

```

optimized by a gradient descent Adam optimizer [36].

The policy network is trained with randomly generated data sets. This is to make reusable on the positions of the probing ports and decap candidates. Details on the random data set generator are explained in the following sub-section and an overall pseudo algorithm for training is shown in Algorithm 1.

D. Random Data Set Generator for Reusability

To train the reusable policy network, a random data set generator is implemented. It generates the data set s and corresponding PDN Z-matrices Z_{PDN} . s is the set of state s consisting of randomly selected 4 probing ports p and n decap candidate ports as shown in Fig. 3(a):

$$\begin{aligned}
 s &= (s_1, s_2, \dots, s_N) \\
 s_k &= (p_k, x_k), k \in \{1, \dots, N\} \\
 Z_{PDN, s} &= (Z_{s1}, Z_{s2}, \dots, Z_{sN}).
 \end{aligned} \tag{19}$$

where N is the number of the data; k indicates the data index; p_k and x_k are defined in (2) and (1) respectively. The p_k and x_k are randomly selected from a full-port Z-parameter model of the HBM VDDQ PDN. The full-port model has total 816 ports on the on-chip and on-interposer PDN since one port is assigned for one UDUC in Fig. 3(a). 48 probing port candidates are in the I/O region (PHY) and 768 decap candidates are in the remaining on-chip and on-interposer PDN. $N=1000, 100$ and 100 are used for training, validation, and test sets respectively.

III. MODELING OF HBM VDDQ PDN FOR RANDOM DATA SET GENERATOR AND REWARD ESTIMATOR

For implementing the random data set generator and reward estimator, a VDDQ PDN model based on the HBM gen 2 and

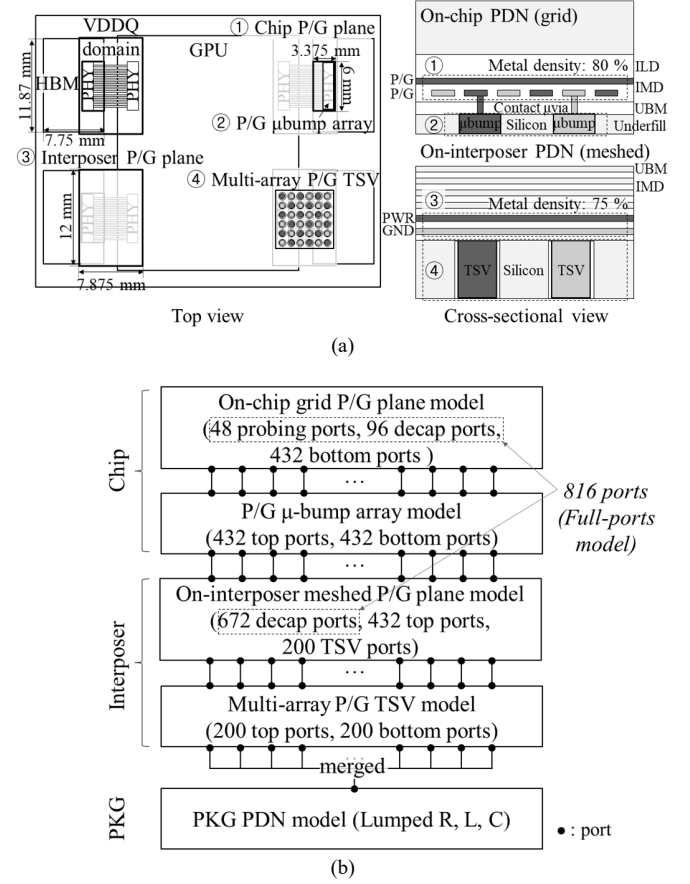


Fig. 7. (a) Configuration of HBM VDDQ PDN for this work. (b) Modeling of hierarchical VDDQ PDN impedance by cascading all the modeled components.

2E is constructed as shown in Fig. 7(a) [37]–[39]. The modeling components considered in this work are as follows: 1) on-chip grid P/G planes, 2) P/G μ bump array with contact μ vias, 3) on-interposer meshed P/G planes, 4) multi-array P/G TSVs, 5) package (PKG) PDN, 6) NMOS decaps. Details on physical dimensions and material properties are summarized in Table I. The whole hierarchical PDN is modeled by cascading all the modeled components as shown in Fig. 7(b). The principle of cascading two Z-matrices is the same as described in Section II-C. All the distributed ports of the on-chip and on-interposer components are cascaded. Since PKG PDN is modeled as the lumped model, all the bottom ports of the multi-array TSV model are merged and cascaded to the PKG PDN.

The on-chip and on-interposer P/G planes are modeled by cascading the UDUCs. The UDUCs are modeled by cascading the UCs. Since the size of the UDUC is the same for both the chip and interposer, the on-chip UDUC is composed of 5625 (75 by 75) on-chip UCs and the on-interposer UDUC is configured of 625 (25 by 25) on-interposer UCs. Through W-element modeling methods, the UCs are modeled in per-UC resistance R_{UC} , inductance L_{UC} , conductance G_{UC} and capacitance C_{UC} as shown in Fig. 8(a) [40], [41]. Both R_{UC} and G_{UC} include DC and AC components (R_0, R_f, G_0, G_f). First, y-direction wave propagation of the UC is modeled. Using a perfect magnetic conductor boundary on the x-direction sides

TABLE I
PHYSICAL DIMENSIONS AND MATERIAL PROPERTIES OF
HBM VDDQ PDN

Objective	Parameter	Description	Value
On-chip P/G plane	$L_{UC, chip}$	Length of on-chip UC	5 [μm]
	$W_{UC, chip}$	Width of on-chip UC	2 [μm]
	$S_{UC, chip}$	Space of on-chip UC	3 [μm]
	$t_{Cu, chip}$	Metal (Copper) thickness	0.5 [μm]
	$h_{Si, chip}$	Height of silicon substrate	30 [μm]
	$h_{IMD, chip}$	Height of IMD layer	0.5 [μm]
	$h_{ILD, chip}$	Height of ILD layer	2 [μm]
On-interposer P/G plane	$L_{UC, interposer}$	Length of on-interposer UC	15 [μm]
	$W_{UC, interposer}$	Width of on-interposer UC	7.5 [μm]
	$S_{UC, interposer}$	Space of on-interposer UC	7.5 [μm]
	$t_{Cu, interposer}$	Metal (Copper) thickness	1 [μm]
	$h_{Si, interposer}$	Height of silicon substrate	100 [μm]
	$h_{IMD, interposer}$	Height of IMD layer	1 [μm]
	$h_{UBM, interposer}$	Height of UBM layer	1 [μm]
μbump array	$d_{μbump}$	Diameter of μbump	25 [μm]
	$h_{μbump}$	Height of μbump	33 [μm]
	$p_{μbump}$	Pwr-to-gnd pitch of μbump	145.6 [μm]
Contact μvia	$d_{μvia}$	Diameter of μvia	2 [μm]
	$h_{μvia}$	Height of μvia	1.5 [μm]
Multi-array P/G TSV	d_{TSV}	Diameter of TSV	15 [μm]
	p_{TSV}	Pitch of TSV	375 [μm]
	t_{SiO_2}	SiO ₂ thickness	0.5 [μm]
Material properties	σ_{Cu}	Conductivity of Cu (P/G metal, μbump, contact μvia)	5.8×10^7 [S/m]
	σ_{Si}	Conductivity of Si substrate	10 [S/m]
	$\epsilon_{IMD, chip}$	Relative permittivity of on-chip IMD layer	3.5 @ 9.0 GHz
	$\epsilon_{ILD, chip}$	Relative permittivity of on-chip ILD layer	4.1 @ 9.0 GHz
	$\epsilon_{UBM, chip}$	Relative permittivity of on-chip UBM layer	6.5 @ 9.4 GHz
	$\epsilon_{underfill, chip}$	Relative permittivity of on-chip underfill	3.2 @ 9.4 GHz
	ϵ_{Si}	Relative permittivity of Si	11.9 @ 10 GHz
	$\epsilon_{IMD, interposer}$	Relative permittivity of on-interposer IMD layer	4.1 @ 9.0 GHz
	$\epsilon_{UBM, interposer}$	Relative permittivity of on-interposer UBM layer	6.5 @ 9.4 GHz
	$\tan\delta_{IMD, chip}$	Loss tangent of on-interposer IMD layer	0.001 @ 9.0 GHz
	$\tan\delta_{ILD, chip}$	Loss tangent of on-chip ILD layer	0.001 @ 9.0 GHz
	$\tan\delta_{UBM, chip}$	Loss tangent of on-chip UBM layer	0.001 @ 9.4 GHz
	$\tan\delta_{underfill, chip}$	Loss tangent of on-chip underfill	0.02 @ 9.4 GHz
	$\tan\delta_{IMD, interposer}$	Loss tangent of on-interposer IMD layer	0.001 @ 9.0 GHz
	$\tan\delta_{UBM, interposer}$	Loss tangent of on-interposer UBM layer	0.001 @ 9.4 GHz

of the UC, a channel-like P/G plane with 2 ports on the other y-direction sides is made [40]. The channel-like P/G plane is simulated by 3-D EM simulator to obtain S-parameter. By assuming the channel-like P/G plane as a W-element transmission line (TL) model, per-length model parameters R_0 , R_f , L , G_0 , G_f and C are extracted from the simulated S-parameter [41]. When extracting frequency-independent parameters R_0 , R_f , G_0 , and G_f from real parts of per-length impedance Z and admittance Y , least-square solutions are derived [41, eq. (6)].

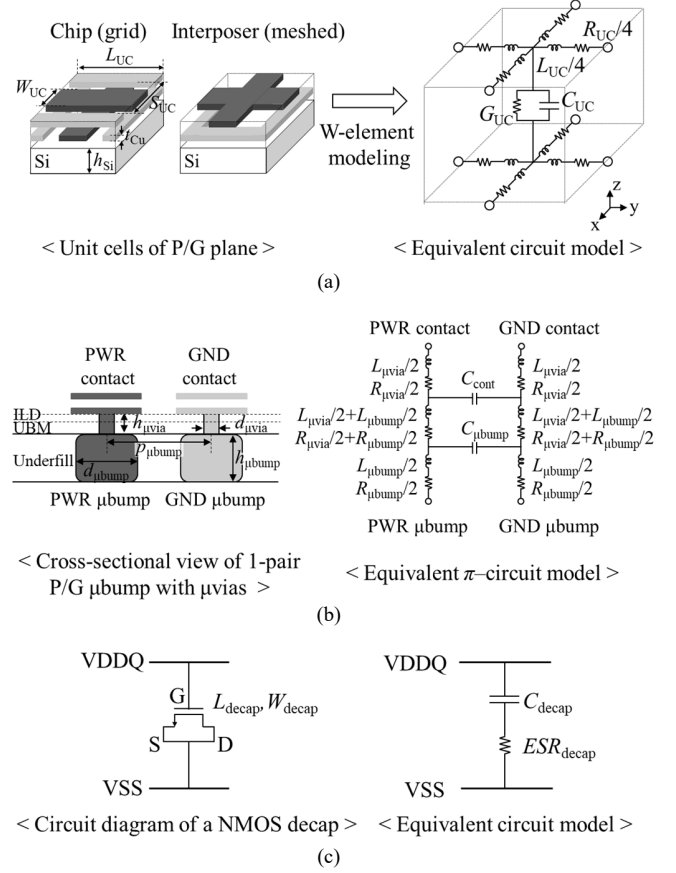


Fig. 8. (a) Modeling of on-chip and on-interposer UC. (b) Modeling of 1-pair P/G μbump with contact μvias. (c) Modeling of NMOS decap.

When extracting frequency-dependent parameters L and C from imaginary parts of Z and Y respectively, the mean of the solutions is derived [41, eq. (9)]. The final UC model is obtained by extending the x-direction model parameters as same as the y-direction.

The μbump array in the HBM VDDQ PDN consists of 432 μbump pairs [37]. The coupling between μbump pairs is assumed to be negligible. Then, the model of μbump array $Z_{μbumpArray}$ is expressed by the extension of that of 1-pair μbumps $Z_{1-pair}(f)$:

$$Z_{μbumpArray} = \begin{bmatrix} Z_{1-pair}(f) & \cdots & \mathbf{0} \\ \vdots & \ddots & \vdots \\ \mathbf{0} & \cdots & Z_{1-pair}(f) \end{bmatrix} \quad (20)$$

where all the diagonal elements are the 2-port $Z_{1-pair}(f)$ and zero-matrices $\mathbf{0}$ otherwise. As shown in Fig. 8(b), the 1-pair μbumps with contact μvias are modeled as the equivalent π-circuit model. Both the μbump and μvia pairs are modeled as cylindrical TLs. Detailed equations for model parameters $R_{μbump}$, $L_{μbump}$, $C_{μbump}$, $R_{μvia}$, $L_{μvia}$, and $C_{μvia}$ are denoted in [42, eqs. (1)–(3)].

The multi-array TSV is configured of 400 P/G TSVs (20 by 20) with the case 2 pattern in [40, Fig. 10]. It is modeled based on the multi-conductor TL modeling method [40], [43]. Detailed equations are denoted in [40, eqs. (26)–(41)].

TABLE II
MODELED PARAMETERS OF THE HBM VDDQ PDN

Objective	Parameter	Value
On-chip P/G plane	$R_{0, \text{chip}} / R_{f, \text{chip}}$	30653.63 / 0.033 [Ω/m]
	L_{chip}	268.36 [nH/m]
	$G_{0, \text{chip}} / G_{f, \text{chip}}$	0 / 1.18×10^{-11} [S/m]
	C_{chip}	430 [pF/m]
On-interposer P/G plane	$R_{0, \text{interposer}} / R_{f, \text{interposer}}$	2699.06 / 0.033 [Ω/m]
	$L_{\text{interposer}}$	120.74 [nH/m]
	$G_{0, \text{interposer}} / G_{f, \text{interposer}}$	0 / 2.05×10^{-11} [S/m]
	$C_{\text{interposer}}$	511.8 [pF/m]
μbump array	$R_{\mu\text{bump}}$	0.01 [Ω] @ 10 GHz
	$L_{\mu\text{bump}}$	8.1 [pH]
	$C_{\mu\text{bump}}$	1.2 [fF]
Contact μvia	$R_{\mu\text{via}}$	0.01 [Ω] @ 10 GHz
	$L_{\mu\text{via}}$	0.75 [pH]
	$C_{\mu\text{via}}$	0.03 [fF]
Unit NMOS decap	$C_{\text{unit decap}}$	1.055 [nF]
	$ESR_{\text{unit decap}}$	0.7 [m Ω]
PKG PDN (Lumped)	R_{PKG}	30 [m Ω]
	L_{PKG}	0.5 [nH]
	C_{PKG}	100 [nF]

The unit NMOS decap for the sub-action a_t is modeled by scaling the model of one NMOS decap. Generally, the NMOS decap is modeled as C_{decap} and ESR_{decap} in series as shown in Fig. 8(c) [42]. The model is based on the TSMC 65 nm process and the parameters L_{decap} and W_{decap} are 0.24 μm and 1 μm respectively. C_{decap} and ESR_{decap} for the decap are extracted by SPICE simulator. Then, $C_{\text{unit decap}}$ and $ESR_{\text{unit decap}}$ are scaled by the number of the decaps in the $375 \times 375 \mu\text{m}^2$ unit area. All the modeled parameters are summarized in Table II.

IV. VERIFICATION OF THE PROPOSED METHOD

In this section, the superiorities of the proposed method is verified by comparing the optimality performance, reusability, scalability, computing time and cost to the previous methods including GA, RS and RL-based methods [21]–[28].

Table III summarizes the hyper-parameter set-up for the transformer network and training. The number of the attention layers in the encoder (L) is set to 3. The dimensions of the input, embed (hidden) and feedforward layers in the encoder (d_x , d_h , d_{ff}) are set to 4, 128, 512 respectively. The dimensions of the context node and hidden layer (d_{hc} , d_h) in the decoder are set to 640 and 128 respectively. The value of tanh clipping (C) is set to 10. The dimensions of the head, key and value (M , d_k , d_v) are set to 8, 16 and 16 for the MHA layers respectively, and 1, 128 and 128 for the SHA layers respectively. The total number of 20 train epochs are trained; one epoch size is 1000; the batch size is 100 and the validation size is 100. The initial learning rate is 10^{-4} and is linearly decayed by 0.95 times every epoch. The proposed method is verified in 12 decap n/m problems with the same hyper-parameter set-up: decap 100/20, 100/30, 100/50, 100/60, 200/20, 200/40, 200/60, 200/100, 300/20, 300/60, 300/90 and 300/150.

A. Training and Validation Loss Convergence Verification

Fig. 9(a) shows the training and validation loss convergence characteristics in 12 decap n/m problems. For every problem,

TABLE III
HYPER-PARAMETER SET-UP FOR THE TRANSFORMER-BASED POLICY NETWORK AND TRAINING

Parameter			Value
Transformer-based Policy Network	Encoder	Attention layer # (L)	3
		Input dim (d_s)	4
		Embed (Hidden) dim (d_h)	128
		Feed forward dim (d_{ff})	512
	Decoder	Context node dim (d_{hc})	640 ($d_h \times 5$)
		Hidden dim (d_h)	128
		tanh clipping (C)	10
		Head dim (M)	
Key, value dim (d_k, d_v)		16 for MHA, 128 for SHA	
Training	Train epoch # (E)		20
	Train epoch size		1000
	Batch size (B)		100
	Validation size (V)		100
	Learning rate		10^{-4}
	Learning rate decay		0.95

training and validation loss converge after about 100 training steps (=100 batches=10 epochs=10000 train data).

Fig. 9(b) and (c) show the performance improvement depending on the training steps in the decap 200/40– the decap optimization results and corresponding self- and transfer impedance of the test data #33. The blue triangles are 4 probing ports, the black circles are the decap candidates and the red circles are the decap assignment in Fig. 9(b). As the training progresses, the policy network assigns unit decaps near the probing ports in both the on-chip and on-interposer PDN. This result coincides with the physical insight. Corresponding one self-impedance Z_{22} and one transfer impedance Z_{23} are plotted in Fig. 9(c). The probing port numbers are denoted starting from the upper port to the lower port in the PHY region. As the training progresses, both the self- and the transfer impedance are reduced furthermore. From 40 MHz to 100 MHz frequency range, differences in the impedance profiles are not noticeable since the capacitance of the assigned decaps dominates. In other words, the number of the assigned unit decaps is the dominant factor. However, spreading loop resistance and inductance dominate in the frequency range over 100 MHz. Those are determined by the positions of assigned unit decaps. Therefore, the results of training step #100 where more unit decaps are assigned closer to the probing ports and between them show more reduced impedance profiles.

B. Optimality Performance Verification of the Proposed Method by Comparison to the Conventional GA and RS

In this sub-section, the optimality performance of the proposed method is compared to the conventional GA and RS. The average rewards of the 100 test data sets are compared in all the 12 decap n/m problems. The 100 test data sets are generated by the random data set generator and are not correlated with the training and the validation sets. For a fair comparison, the reward functions of the GA and RS are set to be the same as the proposed method. Detailed algorithms of the GA and RS are explained in Algorithm 2 and 3 in the

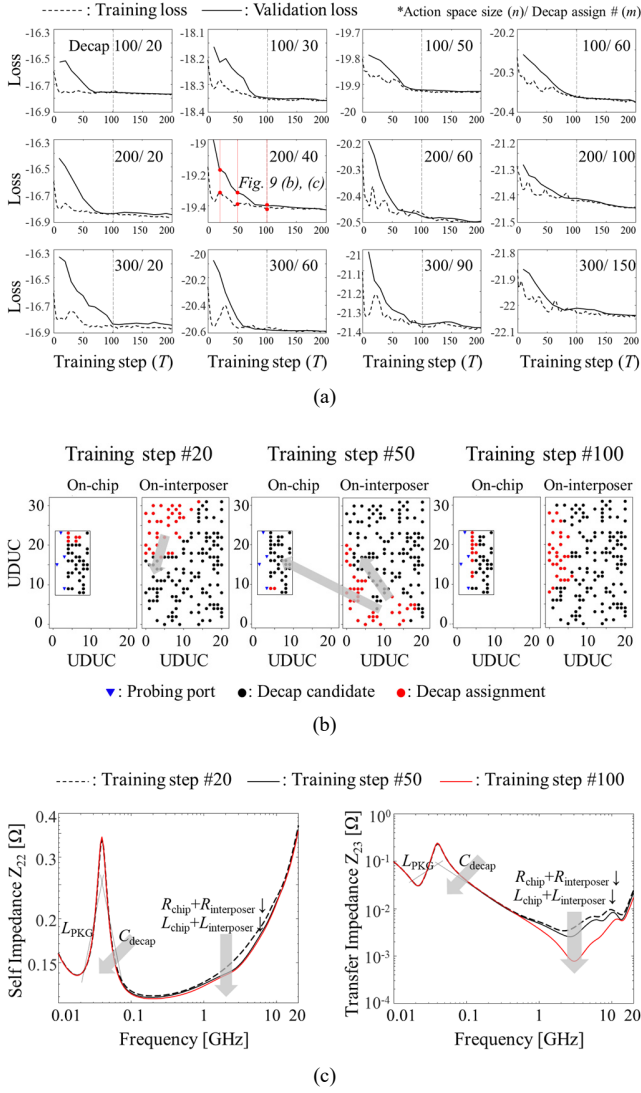


Fig. 9. (a) Training and validation loss convergence characteristics in 12 decap n/m problems. (b) Decap optimization results depending on the training steps in test data #33 of decap 200/40. (c) Self- and transfer-impedance plots depending on the training steps in test data #33 of decap 200/40.

APPENDIX.

Table IV summarizes the average reward comparison results. For the same sampling width of 1000, the proposed method outperforms the GA and RS in all the 12 decap problems. The best performances of the GA are reported among various combinations of the sampling width 1000 by the number of population P and that of the generation $G - \{P \times G\} = \{100 \times 10\}$, $\{50 \times 20\}$, $\{40 \times 25\}$, $\{20 \times 50\}$ and $\{10 \times 100\}$. Moreover, even with 1 sampling width, the average rewards of the proposed method are higher than those of the GA and RS with the sampling width of 1000 in all the problems.

Detailed results of the test data #33 in the decap 200/40 is shown in Fig. 10. The results when all the methods have the sampling width of 1000 are compared – same computing time for the optimization. Fig. 10(a) depicts the decap optimization results. The distribution of the assigned unit decaps is more

TABLE IV
AVERAGE REWARD COMPARISON TO THE CONVENTIONAL GENETIC ALGORITHM (GA) AND RANDOM SAMPLING (RS)

Method		Proposed Method		GA	RS
Problem	Decap num (m)	Sampling width			
		1	1000	1000 {100×10}	1000
100	20	16.780	*16.797	16.751	16.731
	30	18.364	*18.370	18.339	18.326
	50	19.929	*19.934	19.917	19.910
	60	20.381	*20.386	20.361	20.358
200	20	16.849	*16.888	16.808	16.765
	40	19.438	*19.448	19.354	19.329
	60	20.509	*20.515	20.443	20.422
	100	21.459	*21.462	21.420	21.410
300	20	16.874	*16.928	16.836	16.774
	60	20.589	*20.604	20.473	20.440
	90	21.384	*21.390	21.267	21.288
	150	22.055	*22.057	21.979	21.991

*: Best optimality performance

confined near the probing ports for both the on-chip and on-interposer PDN in the proposed method than the GA and RS. Corresponding four self-impedance profiles Z_{11} , Z_{22} , Z_{33} , and Z_{44} and six transfer-impedance profiles Z_{12} , Z_{13} , Z_{14} , Z_{23} , Z_{24} , and Z_{34} are plotted in Fig. 10(b) and (c) respectively. The red lines are the results of the proposed method. The black solid lines are those of the GA and the black dashed lines are those of the RS. For both the self- and transfer impedance, the proposed method suppresses impedance more than the GA and RS, especially in the frequency range from 100 MHz to 20 GHz where loop inductance and resistance are dominant.

C. Reusability and Scalability Verification of the Proposed Method

In this sub-section, the reusability and scalability that lead to the reduction of the computing time and cost are verified in the proposed method.

The average rewards in Table IV are the results of the 100 randomly generated test sets that are not correlated to the training and validation sets. The results by the proposed method show superior performance than the GA and RS. Fig. 11 shows the detailed decap optimization results on four different test data #1, #3, #6 and #21 in the decap 200/40. Regardless of the positions of the probing ports and decap candidates, the reusable policy network provides well-designed results without additional training. Therefore, the transformer-based policy network is reusable on the positions of the probing ports and decap candidates.

Fig. 12(a) shows the verification of the encoder scalability on the size of the action space. Average rewards of the policy network trained in the smaller action space size and that trained in the original action space size are compared. The network trained in decap 100/20 is applied to solve the decap 200/20 and 300/20 problems. For the size of the action space of 200, the average rewards are equal to 16.849 without the sampling decoding strategy. For the size of the action space of 300, the average reward is slightly lower when the sample widths are the same as 1 – 16.862 for the network trained in decap 100/20;

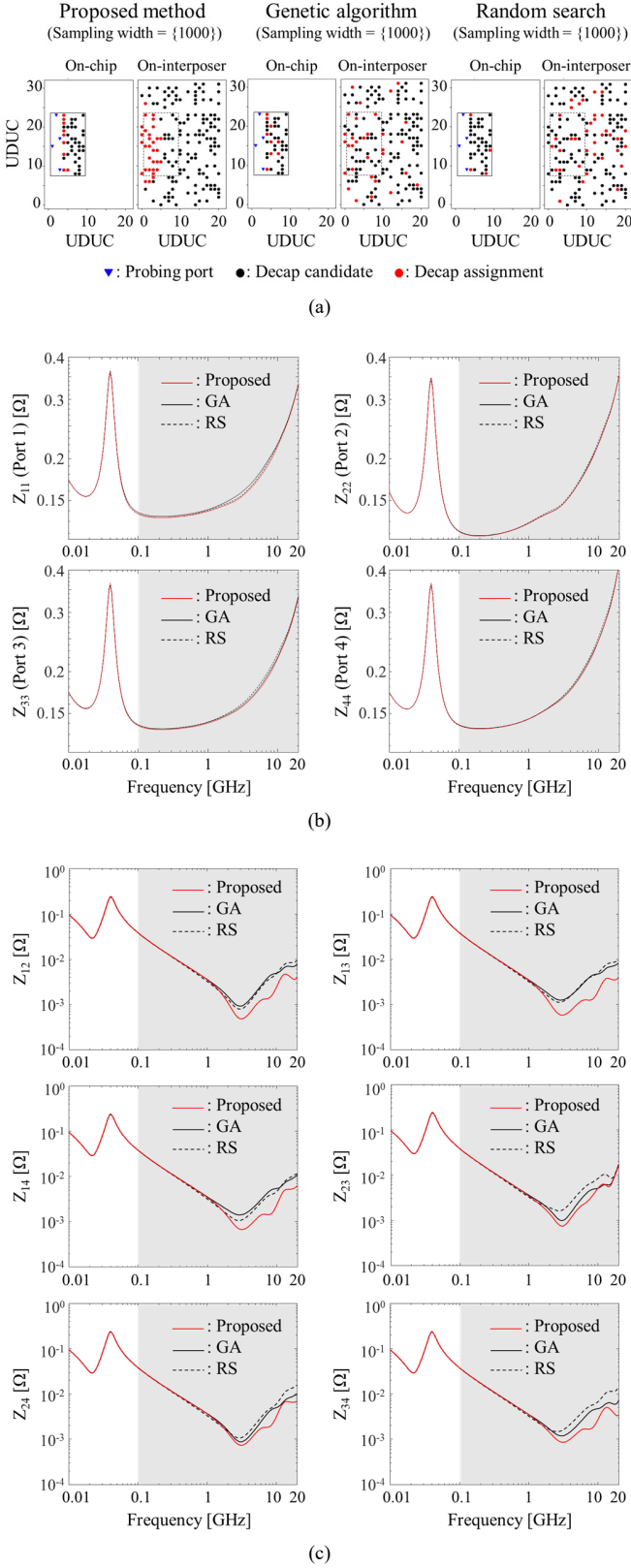


Fig. 10. Optimization results comparison of the test data #33 in the decap 200/40 between the proposed method and the conventional GA and RS with sampling width=1000: (a) Decap optimization results. (b) Four self-impedance profiles seen at probing ports. (c) Six transfer impedance profiles seen at probing ports.

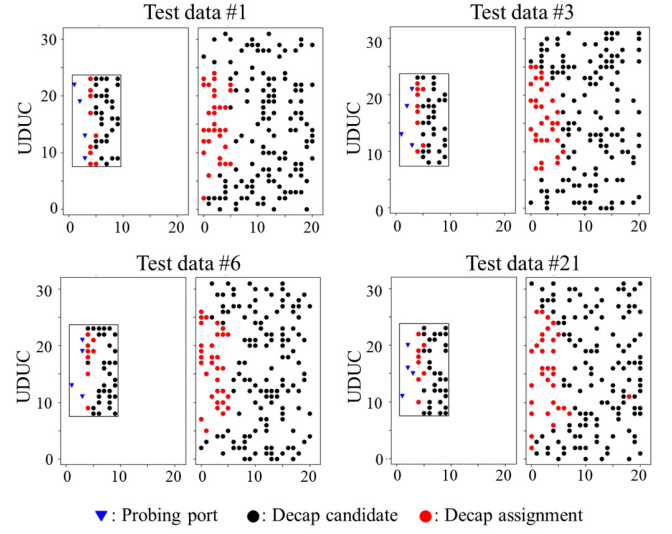


Fig. 11. Reusability verification on positions of the probing ports and decap candidates – decap optimization results of test data #1, #3, #6 and #21 in decap 200/40.

16.874 for the network trained in decap 300/20. However, this gap is not noticeable and can be easily overcome by increasing the sampling width to 10. The average reward of the network trained in decap 100/20 with the sampling width 10 is 16.894. Hence, the network trained in decap 100/20 can adapt to solve the problems that have a larger number of the decap candidates.

Fig. 12(b) depicts the verification of the decoder scalability on the number of the decap assignments. The method is the same as the encoder scalability verification, but sweeping the size of the decap assignments with the fixed action space size. The network trained in decap 100/20 is applied to solve decap 100/30, 50, 60; that trained in decap 200/40 to solve decap 200/60, 100; that trained in decap 300/60 to solve decap 300/100, 150. It is to verify whether the network trained in problems assigning 20 % of the decap candidates is scalable to solve assigning up to 50–60 % of the decap candidates. The results in Fig. 12(b) show the same optimality performance in all the cases. Therefore, the decoder has the scalability on the number of the decap assignments.

D. Computing Time and Cost Comparison to the Conventional GA, RS and Previous RL-based methods

In this sub-section, the computing time and cost of the proposed method are compared with the previous methods. The optimization time and cost are compared between the proposed method, GA and RS. The training time and cost are compared between the proposed method and the previous RL-based methods [21]–[28].

To compare with the GA and RS, a time-performance analysis is performed as shown in Fig. 13. The time-performance analysis is widely used to evaluate the performance improvement of the optimization methods depending on the time or sampling width [33]. The average rewards per sampling width are compared to find out the values of the sampling width to realize the same performance. For

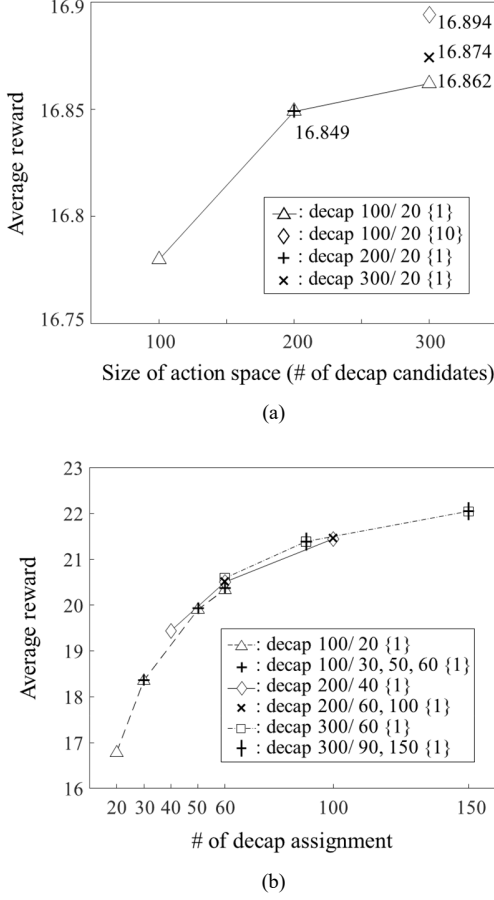


Fig. 12. Verification of the encoder scalability on the size of the action space (# of decap candidates). (b) Verification of the decoder scalability on the number of the decap assignments.

every problem, even with the sampling width of 1000, the GA and RS do not reach the same performance of the proposed method with the sampling width of 1. In other words, the GA and RS need to sample 1000 times more to achieve the same performance. Therefore, more than 1000 times of the computing time and cost are required in the GA and RS. This can be possible because the policy network in the proposed method can consider the sequential relationship between the decap assignments and has reusability. The reusable network can optimize the decap designs for 100 different test data by just one inference per data. Detailed comparison results of the optimization time and cost to realize the same performance are summarized in Table V.

For the previous RL-based methods, we cannot directly compare the results on the decap n/m problems. Because the solution space coverages of the previous methods are limited to solve the decap problems as shown in Table VI. The value-based RL algorithms and their simple value or policy networks such as the MLP and CNN limit the solution space [21]–[26]. Moreover, the previous methods in [21]–[28] cannot consider both the self- and transfer impedance for the design metric. The methods in [21]–[25], [27], [28] are limited to just one probing port. In addition, the methods in [21]–[27] do not have reusability since the value or policy networks are trained in one

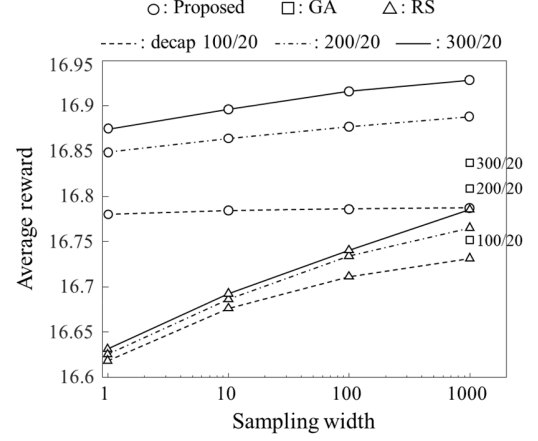


Fig. 13. Time-performance analysis on the proposed method and conventional GA and RS-based optimization methods.

TABLE V
COMPARISON OF OPTIMIZATION TIME AND COST FOR SAME PERFORMANCE BETWEEN THE PROPOSED METHOD, GA AND RS

Problem	Method	Proposed Method {1}	GA {1000 >}	RS {1000 >}
Decap 100/20	Time	11 s	3 h >	3 h >
	Cost	2.8 GB	2.8 TB >	2.8 TB >
Decap 200/20	Time	57 s	16 h >	16 h >
	Cost	10.8 GB	10.8 TB >	10.8 TB >
Decap 300/20	Time	2m 16s	1d 14h >	1d 14h >
	Cost	24.6 GB	24.6 TB >	24.6 TB >

* Total optimization time = $1t \times \text{sampling width}$, total cost = $1dc \times \text{sampling width}$
 * $1t$ = optimization time for 100 test data, $1dc$ = data cost of 100 test data
 * CPU: Intel Xeon(R) Silver 4210R @2.4 GHz, GPU: NVIDIA GeForce RTX 3090, RAM: DDR4 512 GB

PDN data. The networks always must be re-trained whenever a new different PDN data is given. Therefore, their optimization time includes the training time, causing a significant increment of the total computing time than the reusable proposed method.

The previous methods in [21]–[28] are limited in the scalability. Those must train the value or policy networks in the same scale of the decap problems that they intend to solve. Therefore, the training time and data cost are critically larger compared to the scalable proposed method. It is proved by comparing the training time and data cost depending on the encoder and decoder scalability of the proposed method. Table VII shows the comparison results. The results are based on the scalability verification in Fig. 12(a) and (b) of Section IV-C. The data cost is the size of the 1000 training and 100 validation data.

The encoder scalability can reduce both the training time and data cost. Because the size of the VDDQ PDN Z-matrix for the training can be significantly reduced. It leads to the decrement of the execution time for cascading the VDDQ PDN and decap array. The reduction ratio of the training time between decap 100/20 and 200/20 is 80.7 %. That between decap 100/20 and 300/20 is 91.9 %. The reduction ratios of the data cost are 74.1 % and 88.6 % respectively.

The decoder scalability can also reduce the training time because the size of the decap array Z-matrix is reduced. It effects the execution time for cascading. The reduction ratio of the training time between decap 100/20 and 60, that between

TABLE VI
COMPARISON BETWEEN THE PROPOSED METHOD AND
PREVIOUS RL-BASED METHODS

Method	Reusability	Scalability	RL type	NN	Solution space	Metric	Multi probe
Proposed	Yes	Yes	P	Transformer	1×10^{89}	Z_{11}/Z_{21}	Yes
[21]	No	No	V	-	6.6×10^4	Z_{11}	No
[22]	No	No	V	-	3.2×10^9	Z_{11}	No
[23]	No	No	V	MLP	1×10^5	Z_{11}	No
[24]	No	No	V	CNN	1.4×10^{17}	Z_{11}	No
[25]	No	No	V	MLP	1×10^{14}	Z_{11}	No
[26]	No	No	P	MLP	3.4×10^{32}	Z_{11}	Yes
[27]	No	No	P	Transformer	1×10^{60}	Z_{11}	No
[28]	Yes	No	P	Ptr net	8.2×10^{18}	Z_{11}	No

*P: Policy, V: Value, NN: neural network for value/policy approximation, Ptr net: pointer network

TABLE VII
COMPARISON OF TRAINING TIME AND DATA COST
DEPENDING ON THE ENCODER AND DECODER SCALABILITY

	Action Space	Model (Trained in)	Train time [s]	Data cost [GB]
Encoder	200	100/20	2200	30.8
		200/20	11400	118.8
		Reduction	80.7 %	74.1 %
	300	100/20	2200	30.8
		300/20	27200	270.6
		Reduction	91.9 %	88.6 %
Decoder	100	100/20	2200	30.8
		100/60	3800	30.8
		Reduction	42.1 %	0 %
	200	200/40	11400	118.8
		200/100	25200	118.8
		Reduction	54.8 %	0 %
	300	300/60	66400	270.6
		300/150	104800	270.6
		Reduction	36.6 %	0 %

*Data cost: size of train/validation data sets

decap 200/40 and 100 and that between decap 300/60 and 150 are 42.1 %, 54.8 % and 36.6 % respectively. Therefore, assuming that the solution space coverages of the previous RL methods are large enough and have reusability, the encoder and decoder scalabilities of the proposed method can significantly reduce the training time and data cost compared to the previous non-scalable methods [21]–[28].

V. CONCLUSION

In this article, for the first time, we propose a transformer network-based RL method for the PDN decap optimization of HBM. The ability to capture sequential relations of the decap assignments, reusability and scalability realize superiorities on the optimality performance, computing time and cost, compared to the conventional GA, RS and the previous RL-based methods. In addition, the proposed method considers both the self- and transfer impedance seen at the multiple ports as optimization metrics. Therefore, we demonstrate the feasibility of the RL-based method in designing practical PDNs such as the HBM VDDQ PDN.

Algorithm 2 GA for PDN decap optimization (decap n/m)

Inputs: action space size n , number of decap assignments m , number of initial population P , number of generations G , state of a test PDN s , Z-matrix of a test PDN Z_s , Z-matrix of m -sized unit decap array Z_{da}

Initialize $g = 0$

$ch^0 \leftarrow \text{RandomPopulation}(n, m, P)$

$r_i^0 \leftarrow \text{RewardEst}(ch_i^0, s, Z_s, Z_{da}) \forall i \in \{1, \dots, P\}$

$ch^0 \leftarrow \text{Sort}(ch^0, r^0)$

$sel^0 \leftarrow \text{Selection}(\alpha, ch^0)$

$elite^0 \leftarrow \text{Selection}(e, ch^0)$

for $g = 0$ to $G - 1$ do

$lssel^g \leftarrow \{sel_1^g[0 : n/2], \dots, sel_P^g[0 : n/2]\}$

$rssel^g \leftarrow \{sel_1^g[n/2 + 1 : -1], \dots, sel_P^g[n/2 + 1 : -1]\}$

$ch^{g+1} \leftarrow \{elite^g, \text{Crossover}(lssel^g, rssel^g)\}$

if $\text{rand}() < \beta$ then

$ch_i^{g+1} \leftarrow \text{Mutation}(ch_i^{g+1}) \forall i \in \{1, \dots, P\}$

endif

$r_i^{g+1} \leftarrow \text{RewardEst}(ch_i^{g+1}, s, Z_s, Z_{da}) \forall i \in \{1, \dots, P\}$

$ch^{g+1} \leftarrow \text{Sort}(ch^{g+1}, r^{g+1})$

$\alpha \leftarrow \alpha \times d$

$sel^{g+1} \leftarrow \text{Selection}(\alpha, ch^{g+1})$

$elite^{g+1} \leftarrow \text{Selection}(e, ch^{g+1})$

end for

return $\text{argmax}_{ch^{g+1}}(\tau^{g+1}), \text{max}(r^{g+1})$

Algorithm 3 RS for PDN decap optimization (decap n/m)

Inputs: action space size n , number of decap assignments m , sampling width N , state of a test PDN s , Z-matrix of a test PDN Z_s , Z-matrix of m -sized unit decap array Z_{da}

$ch \leftarrow \text{RandomPopulation}(n, m, N)$

$r_i \leftarrow \text{RewardEst}(ch_i, s, Z_s, Z_{da}) \forall i \in \{1, \dots, N\}$

return $\text{argmax}_{ch}(r), \text{max}(r)$

APPENDIX

Detailed pseudo algorithms of the GA and RS for the decap n/m problem are described in Algorithm 2 and 3 respectively. Detailed definitions of variables and functions in the GA are as follows:

1) Variables in the GA

- P : number of initial populations.
- G : number of generations.
- s : state of a test PDN.
- Z_s : Z-matrix of a test PDN.
- Z_{da} : Z-matrix of m -sized unit decap array.
- ch^g : a set of P number of g -th generation chromosomes $\{ch_1^g, \dots, ch_P^g\}$.
- ch_i^g : an i -th chromosome in ch^g consisting of n number of binary genes – 1: decap assigned, 0: no decap.
- r^g : a set of rewards of g -th generation chromosomes $\{r_1^g, \dots, r_P^g\}$.
- r_i^g : a reward of the i -th chromosome in r^g .

- j) α : ratio of selection for the next generation (=0.5 for this work).
 - k) sel^g : a set of selected top $\alpha \times 100$ % of g -th generation chromosomes $\{sel_1^g, \dots, sel_p^g\}$.
 - l) e : ratio of elite chromosome selection for the next generation (=0.1 for this work).
 - m) $elite^g$: a set of selected top $e \times 100$ % elite chromosomes which are remained without crossover.
 - n) $lset^g$: a set of left halves of the selected chromosomes in sel^g .
 - o) $rset^g$: a set of right halves of the selected chromosomes in sel^g .
 - p) β : probability to perform mutation (=0.05 for this work).
 - q) d : ratio of decaying the selection ratio α every generation (=0.95 for this work).
- 2) **Functions in the GA**
- a) RandomPopulation(n, m, P): Random generation of P number of n -sized chromosomes with m number of 1-assigned genes.
 - b) RewardEst(ch_i^g, s, Z_s, Z_{da}): Reward estimator described in Section II-C.
 - c) Sort(ch^g, r^g): Sorting the chromosomes in ch^g according to the reward r^g .
 - d) Selection(α, ch^g): Selecting top $\alpha \times 100$ % of g -th generation chromosomes
 - e) Crossover($lset^g, rset^g$): Generating $(1 - e) \times P$ number of random combinations between $lset^g, rset^g$.
 - f) Mutation(ch_i^g): Exchanging two 0-assigned and 1-assigned genes.

The only different variable in the RS is a sampling width N which indicates the number of population P in the GA. Other variables and functions in the RS are the same as those explained in the GA.

ACKNOWLEDGMENT

We would like to acknowledge the technical support from ANSYS Korea.

REFERENCES

- [1] J. U. Knickerbocker *et al.*, "3D silicon integration," *2008 58th Electronic Components and Technology Conference*, 2008, pp. 538-543.
- [2] M. Min and S. Kadivar, "Accelerating Innovations in the New Era of HPC, 5G and Networking with Advanced 3D Packaging Technologies," *2020 International Wafer Level Packaging Conference (IWLPAC)*, 2020, pp. 1-6.
- [3] B. Koo, S. Lee, K. Chae and J. Kim, "Industry-leading high bandwidth memory interface solutions for Inference/AI," in *Proc. DesignCon*, Santa Clara, CA, USA, Jan. 2020.
- [4] J. C. Lee *et al.*, "High bandwidth memory(HBM) with TSV technique," *2016 International SoC Design Conference (ISODC)*, 2016, pp. 181-182.
- [5] K. Cho *et al.*, "Signal Integrity Design and Analysis of Silicon Interposer for GPU-Memory Channels in High-Bandwidth Memory Interface," in *IEEE Transactions on Components, Packaging and Manufacturing Technology*, vol. 8, no. 9, pp. 1658-1671, Sept. 2018.
- [6] D. Yang, J. Xie, M. Swaminathan, X. Wei and E. Li, "A Rigorous Model for Through-Silicon Vias With Ohmic Contact in Silicon Interposer," in *IEEE Microwave and Wireless Components Letters*, vol. 23, no. 8, pp. 385-387, Aug. 2013.
- [7] T. Kim, C. Jo and S. Moon, "Signal Integrity(SI) aware HBM2e/3 interposer design approach considering y-axis offset between logic and HBM die for HPC/AI/Network applications," *2021 IEEE 71st Electronic Components and Technology Conference (ECTC)*, 2021, pp. 1270-1275.
- [8] N. Chatterjee *et al.*, "Architecting an Energy-Efficient DRAM System for GPUs," *2017 IEEE International Symposium on High Performance Computer Architecture (HPCA)*, 2017, pp. 73-84.
- [9] X. C. Wei, Z. Z. Oo, E. Liu and E. Li, "Power integrity analysis of TSV based 3-D integrated circuits," *2012 International Conference on Microwave and Millimeter Wave Technology (ICMMT)*, Shenzhen, 2012, pp. 1-4.
- [10] C. Hwang, J. Kim, B. Achkir and J. Fan, "Analytical Transfer Functions Relating Power and Ground Voltage Fluctuations to Jitter at a Single-Ended Full-Swing Buffer," in *IEEE Transactions on Components, Packaging and Manufacturing Technology*, vol. 3, no. 1, pp. 113-125, Jan. 2013.
- [11] T. Shin *et al.*, "Modeling and Analysis of System-Level Power Supply Noise Induced Jitter (PSIJ) for 4 Gbps High Bandwidth Memory (HBM) I/O Interface," *2021 IEEE Electrical Design of Advanced Packaging and Systems (EDAPS)*, 2021.
- [12] Z. Xu, Z. Wang, Y. Sun, C. Hwang, H. Delingette and J. Fan, "Jitter-Aware Economic PDN Optimization With a Genetic Algorithm," in *IEEE Transactions on Microwave Theory and Techniques*, vol. 69, no. 8, pp. 3715-3725, Aug. 2021.
- [13] W. Shi, Y. Zhou and S. Sudhakaran, "Power delivery network design and modeling for High Bandwidth Memory (HBM)," *2016 IEEE 25th Conference on Electrical Performance Of Electronic Packaging And Systems (EPEPS)*, San Diego, CA, 2016, pp. 3-6.
- [14] H. T. To, N. Na, A. Wong, H. Ke, A. K. Sharma and W. H. Moo, "Top-Down Jitter Specification Approach for HBM System Optimization," in *Proc. DesignCon*, Santa Clara, CA, USA, Jan. 2019.
- [15] M. Popovich, M. Sotman, A. Kolodny and E. G. Friedman, "Effective Radii of On-Chip Decoupling Capacitors," in *IEEE Transactions on Very Large Scale Integration (VLSI) Systems*, vol. 16, no. 7, pp. 894-907, July 2008.
- [16] S. Piersanti, F. de Paulis, C. Olivieri and A. Orlandi, "Decoupling Capacitors Placement for a Multichip PDN by a Nature-Inspired Algorithm," in *IEEE Transactions on Electromagnetic Compatibility*, vol. 60, no. 6, pp. 1678-1685, Dec. 2018.
- [17] J. Wang, Z. Xu, X. Chu, J. Lu, B. Ravelo and J. Fan, "Multiport PDN Optimization With the Newton-Hessian Minimization Method," in *IEEE Transactions on Microwave Theory and Techniques*, vol. 69, no. 4, pp. 2098-2109, April 2021.
- [18] K. Koo, G. R. Luevano, T. Wang, S. Özbayat, T. Michalka and J. L. Drewniak, "Fast Algorithm for Minimizing the Number of decap in Power Distribution Networks," in *IEEE Transactions on Electromagnetic Compatibility*, vol. 60, no. 3, pp. 725-732, June 2018.
- [19] J. Y. Choi and M. Swaminathan, "Decoupling Capacitor Placement in Power Delivery Networks Using MFEM," in *IEEE Transactions on Components, Packaging and Manufacturing Technology*, vol. 1, no. 10, pp. 1651-1661, Oct. 2011.
- [20] M. Swaminathan, H. M. Torun, H. Yu, J. A. Hejase and W. D. Becker, "Demystifying Machine Learning for Signal and Power Integrity Problems in Packaging," in *IEEE Transactions on Components, Packaging and Manufacturing Technology*, vol. 10, no. 8, pp. 1276-1295, Aug. 2020.
- [21] H. Park *et al.*, "Reinforcement Learning-Based Optimal on-Board Decoupling Capacitor Design Method," *2018 IEEE 27th Conference on Electrical Performance of Electronic Packaging and Systems (EPEPS)*, 2018, pp. 213-215.
- [22] J. Shin *et al.*, "Reinforcement Learning-Based Decap Optimization Method for High-Performance Solid-State Drive," *2021 IEEE International Joint EMC/SI/PI and EMC Europe Symposium*, 2021, pp. 718-721.
- [23] L. Zhang *et al.*, "Decoupling Capacitor Selection Algorithm for PDN Based on Deep Reinforcement Learning," *2019 IEEE International Symposium on Electromagnetic Compatibility, Signal & Power Integrity (EMC+SIPI)*, 2019, pp. 616-620.
- [24] H. Park *et al.*, "Deep Reinforcement Learning-Based Optimal Decoupling Capacitor Design Method for Silicon Interposer-Based 2.5-D/3-D ICs," in *IEEE Transactions on Components, Packaging and Manufacturing Technology*, vol. 10, no. 3, pp. 467-478, March 2020.
- [25] L. Zhang, W. Huang, J. Juang, H. Lin, B. -C. Tseng and C. Hwang, "An Enhanced Deep Reinforcement Learning Algorithm for Decoupling Capacitor Selection in Power Distribution Network Design," *2020 IEEE*

International Symposium on Electromagnetic Compatibility & Signal/Power Integrity (EMCSI), 2020, pp. 245-250.

- [26] S. Han, O. W. Bhatti and M. Swaminathan, "Reinforcement Learning for the Optimization of Decoupling Capacitors in Power Delivery Networks," *2021 IEEE International Joint EMC/SI/PI and EMC Europe Symposium*, 2021, pp. 544-548.
- [27] H. Park *et al.*, "Policy Gradient Reinforcement Learning-based Optimal Decoupling Capacitor Design Method for 2.5-D/3-D ICs using Transformer Network," *2020 IEEE Electrical Design of Advanced Packaging and Systems (EDAPS)*, 2020, pp. 1-3.
- [28] H. Kim *et al.*, "Deep Reinforcement Learning Framework for Optimal Decoupling Capacitor Placement on General PDN with an Arbitrary Probing Port," *2021 IEEE 30th Conference on Electrical Performance of Electronic Packaging and Systems (EPEPS)*, 2021, pp. 1-3.
- [29] R. S. Sutton and A. G. Barto, *Reinforcement Learning: An Introduction*. Cambridge, MA, USA: MIT Press, 1998.
- [30] A. Vaswani *et al.*, "Attention is all you need," in *Advances in Neural Information Processing Systems 30*, 2017, pp. 5998-6008.
- [31] W. Kool *et al.*, "Attention, learn to solve routing problems!", in *International Conference on Learning Representations*, 2019.
- [32] K. He, X. Zhang, S. Ren, and J. Sun, "Deep residual learning for image recognition," 2015, *arXiv:1512.03385*.
- [33] I. Bello, H. Pham, Q. V. Le, M. Norouzi and S. Bengio, "Neural combinatorial optimization with reinforcement learning," 2016, *arXiv:1611.09940*.
- [34] R. J. Williams, "Simple statistical gradient-following algorithms for connectionist reinforcement learning," *Machine Learning*, vol. 8, pp. 229-256, 1992.
- [35] Y. Kim *et al.*, "Segmentation method based modeling and analysis of a glass package power distribution network (PDN)", in *Nonlinear Theory and Its Applications, IEICE*, vol. 11, no. 2, pp. 170-188, 2020.
- [36] D. P. Kingma and J. L. Ba, "Adam: A method for stochastic optimization," in *International Conference on Learning Representations*, 2019.
- [37] *High Bandwidth Memory (HBM) Dram*, Standard JESD235, 2013.
- [38] S. Kim *et al.*, "Signal Integrity and Computing Performance Analysis of a Processing-In-Memory of High Bandwidth Memory (PIM-HBM) Scheme," in *IEEE Transactions on Components, Packaging and Manufacturing Technology*, vol. 11, no. 11, pp. 1955-1970, Nov. 2021.
- [39] K. Son *et al.*, "A Novel Through Mold Plate (TMP) for Signal and Thermal Integrity Improvement of High Bandwidth Memory (HBM)," *2020 IEEE MTT-S International Conference on Numerical Electromagnetic and Multiphysics Modeling and Optimization (NEMO)*, 2020, pp. 1-4.
- [40] K. Cho *et al.*, "Fast and Accurate Power Distribution Network Modeling of a Silicon Interposer for 2.5-D/3-D ICs With Multiairray TSVs," in *IEEE Transactions on Components, Packaging and Manufacturing Technology*, vol. 9, no. 9, pp. 1835-1846, Sept. 2019.
- [41] J. He *et al.*, "Extracting characteristic impedance of a transmission line referenced to a meshed ground plane," *2016 IEEE International Symposium on Electromagnetic Compatibility (EMC)*, 2016, pp. 651-656.
- [42] K. Kim *et al.*, "Modeling and Analysis of a Power Distribution Network in TSV-Based 3-D Memory IC Including P/G TSVs, On-Chip Decoupling Capacitors, and Silicon Substrate Effects," in *IEEE Transactions on Components, Packaging and Manufacturing Technology*, vol. 2, no. 12, pp. 2057-2070, Dec. 2012.
- [43] K. Kim *et al.*, "Deep Reinforcement Learning-based Through Silicon Via (TSV) Array Design Optimization Method considering Crosstalk," *2020 IEEE Electrical Design of Advanced Packaging and Systems (EDAPS)*, 2020, pp. 1-3.



Hyunwook Park received the B.S. and M.S. degrees in electrical engineering from the Korea Advanced Institute of Science and Technology (KAIST), Daejeon, Korea, in 2017 and 2019, respectively. He is currently working toward the Ph.D. degree in electrical engineering at KAIST. His current research interests include machine learning-based signal integrity (SI) and power integrity (PI) co-design for 2.5-D/3-D ICs including high bandwidth memory (HBM).



Minsu Kim received a dual degree of B.S. in Mathematics and Computer Science from the Korea Advanced Institute of Science and Technology (KAIST), Daejeon, South Korea, in 2020. He is M.S. candidate in Electrical Engineering, KAIST. His current research interests include Reinforcement Learning (RL) application to channel routing considering signal integrity (SI).



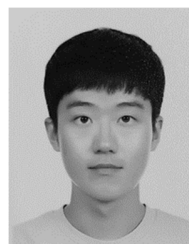
Seongguk Kim received the B.S. degree in electrical engineering from the Korea University, Seoul, South Korea, in 2018 and M.S. degree in electrical engineering from Korea Advanced Institute of Science and Technology (KAIST), Daejeon, Korea, in 2020, where he is currently pursuing the Ph.D. degree. His current research interests include signal and power integrity design and analysis in a processing-in-memory (PIM) system based on high-bandwidth memory (HBM).



Keunwoo Kim received the B.S. and M.S. degree in electrical engineering from the Korea Advanced Institute of Science and Technology (KAIST), Daejeon, South Korea, in 2019 and 2021, respectively, where he is currently pursuing the Ph.D. degree. His current research interests include the reinforcement learning-based signal integrity (SI) and power integrity (PI) design for 2.5-D/3-D ICs.



Haeyeon Kim received her B.S. degree in Electrical Engineering from the Korea Advanced Institute of Science and Technology (KAIST), Daejeon, South Korea, in 2020. She is currently a M.S. candidate in Electrical Engineering, KAIST. Her research interests include Machine Learning (ML) application to Power Distribution Network (PDN) design for 2.5-D/3-D ICs.



Taein Shin received the B.S. degree in mechanical engineering from the Gwangju Institute of Science and Technology (GIST), Gwangju, South Korea, in 2018 and M.S in electrical engineering from Korea Advanced Institute of Science and Technology (KAIST), Daejeon, Korea, in 2020, where he is currently pursuing the Ph.D. degree. His current research includes the modeling, analysis and optimization of High Bandwidth Memory (HBM) I/O interface using machine-learning for power supply noise induced jitter reduction.



Keeyoung Son received the B.S. degree in mechanical engineering from the Korea Advanced Institute of Science and Technology (KAIST), Daejeon, South Korea, in 2019 and the M.S. degree in electrical engineering from KAIST, in 2021, where he is currently pursuing the Ph.D. degree. His current research interests include the signal integrity (SI) and thermal integrity (TI) co-design and analysis for 2.5-D/3-D ICs.



Boogyo Sim received the B.S. degree in electrical engineering from the Korea Advanced Institute of Science and Technology (KAIST), Daejeon, Korea and the M.S. degree in electrical engineering from KAIST, in 2017, 2019, respectively, and is currently working toward the Ph.D. degree in electrical engineering at KAIST. His current research interests are design, analyze and modeling of the wireless power transfer system with high efficiency and low electromagnetic interference.



Subin Kim received the B.S., M.S. and Ph. D. degrees in electrical engineering from the Korea Advanced Institute of Science and Technology (KAIST), Daejeon, Korea, in 2015, 2017, and 2021, respectively.

He has research experience more than six years in the field of power integrity on active interposer based 2.5D/3D-ICs. He is currently with the Global Technology Center, Samsung Electronics, Suwon, Korea. He has authored or coauthored 46 journal and

conference papers. His current research interests include active interposer and integrated voltage regulator design.



Seungtaek Jeong (Member, IEEE) received his B.E. degree in electrical and electronic engineering (with First Class Honors) in 2014 from the University of Auckland, Auckland, New Zealand, and the M.S and Ph.D degrees in electrical engineering in 2017 and 2020 respectively from Korea Advanced Institute of Science and Technology (KAIST), Daejeon, Korea. He is currently a post-doctoral researcher in the Electromagnetic Compatibility laboratory in Missouri Science and Technology, MO, USA. His current research interests include modeling of

electromagnetic interference and signal/power integrity analysis for high-speed interconnects.



Chulsoon Hwang (S'08-M'13-SM'18) received the B.S., M.S., and Ph.D. degrees in electrical engineering from the Korea Advanced Institute of Science and Technology (KAIST), Daejeon, South Korea, in 2007, 2009, and 2012, respectively.

He was with Samsung Electronics, Suwon, South Korea, as a Senior Engineer from 2012 to 2015. In July 2015, he joined the Missouri University of Science and Technology (formerly University of Missouri-Rolla), Rolla, MO, USA, where he is currently an Assistant Professor. His research

interests include RF desense, signal/power integrity in high-speed digital systems, EMI/EMC, hardware security and machine learning.

Dr. Hwang was a recipient of the AP-EMC Young Scientist Award, the Google Faculty Research Award, and Missouri S&T's Faculty Research Award. He was a co-recipient of the IEEE EMC Best Paper Award, the AP-EMC Best Paper Award, and a two-time co-recipient of the DesignCon Best Paper Award.



Jounggho Kim (SM'14-F'18) received the B.S. and M.S. degrees from Seoul National University, Seoul, South Korea, in 1984 and 1986, respectively, and the Ph.D. degree from the University of Michigan, Ann Arbor, MI, USA, in 1993, all in electrical engineering. He joined the Memory Division, Samsung Electronics, Suwon, South Korea, in 1994, where he was involved in gigabit-scale DRAM design. In 1996, he joined Korea Advanced Institute of Science and Technology (KAIST), Daejeon, South Korea. He is currently a Professor with the Department of Electrical

Engineering, KAIST. He is also the Director of the 3-D Integrated Circuit (IC) Research Center supported by SK Hynix, Inc., Icheon, South Korea, and the Smart Automotive Electronics Research Center supported by KET, Inc., Icheon, South Korea. He has given more than 219 invited talks and tutorials in academia and related industries. He has authored or coauthored more than 404 technical papers in refereed journals and conference proceedings. He has authored a book entitled Electrical Design of Through-Silicon-Via (Springer, 2014). In particular, his major research interests include chip package printed circuit board (PCB) codesign and cosimulation for signal integrity, power integrity, ground integrity, timing integrity, and radiated emission in 3D-IC, through-silicon via (TSV), and interposer. His current research interests include electromagnetic compatibility (EMC) modeling, design, and measurement methodologies of 3D-IC, TSV, interposer, system-in package, multilayer PCB, and wireless power transfer (WPT) technology for 3D-IC.